

Assessing Li accommodation at amorphous ZrO₂ grain boundaries

Stephens, Gareth Frank; London, Imperial; Ghardi, Mehdi; Fraile, Alberto; Rushton, Michael; Lee, Bill; Cole-Baker, Aidan; Middleburgh, Simon

Journal of Nuclear Materials

DOI:

<https://doi.org/10.1016/j.jnucmat.2023.154780>

Published: 01/01/2024

Publisher's PDF, also known as Version of record

[Cyswllt i'r cyhoeddiad / Link to publication](#)

Dyfyniad o'r fersiwn a gyhoeddwyd / Citation for published version (APA):

Stephens, G. F., London, I., Ghardi, M., Fraile, A., Rushton, M., Lee, B., Cole-Baker, A., & Middleburgh, S. (2024). Assessing Li accommodation at amorphous ZrO₂ grain boundaries. *Journal of Nuclear Materials*, Article 154780. <https://doi.org/10.1016/j.jnucmat.2023.154780>

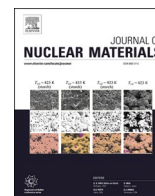
Hawliau Cyffredinol / General rights

Copyright and moral rights for the publications made accessible in the public portal are retained by the authors and/or other copyright owners and it is a condition of accessing publications that users recognise and abide by the legal requirements associated with these rights.

- Users may download and print one copy of any publication from the public portal for the purpose of private study or research.
- You may not further distribute the material or use it for any profit-making activity or commercial gain
- You may freely distribute the URL identifying the publication in the public portal ?

Take down policy

If you believe that this document breaches copyright please contact us providing details, and we will remove access to the work immediately and investigate your claim.



Assessing Li accommodation at amorphous ZrO₂ grain boundaries

Gareth F. Stephens^{a,*}, Megan W. Owen^b, El Mehdi Ghardi^a, Alberto Fraile^a, Susan Ortner^c, Michael J.D. Rushton^a, William E. Lee^a, Aidan Cole-Baker^a, Simon C. Middleburgh^a

^a Nuclear Futures Institute, Bangor University, Bangor, LL57 1UT, UK

^b Department of Materials, Imperial College London, London, SW7 2AB, UK

^c National Nuclear Laboratory, Culham Science Centre, Abingdon, Oxfordshire, OX14 3DB, UK

HIGHLIGHTS

- Lithium is known to accelerate the corrosion of zirconium alloy.
- Complex grain boundaries can be considered amorphous.
- Defect concentrations are predicted for amorphous zirconia.
- Oxide/water interface partial pressure of oxygen is predicted.
- Brouwer diagrams highlight predicted defect concentrations.
- The solubility of Li into amorphous ZrO₂ is found to be possible.

ARTICLE INFO

Keywords:

ZrO₂ Brouwer Diagram
lithium accelerated corrosion
Lithium solubility in ZrO₂
Complex grain boundaries amorphous zirconia
Zirconia defect concentration

ABSTRACT

Nuclear Pressurised Water Reactors (PWRs) use zirconium alloys as a fuel cladding, preventing the cooling water, at elevated pH using lithium hydroxide, from interacting with the fuel. Boron, as boric acid, is added to the coolant as a reactivity shim. Future reactor designs are considering removing soluble boron reactivity control to aid plant simplification. The presence of lithium in the absence of boron in the coolant has, however, been found to accelerate the corrosion of zirconium-based alloys under certain conditions and the mechanisms by which this occurs is under investigation. The ingress of lithium into the bulk oxide layer of zirconium alloy has been addressed in a previous study and was found to be unlikely. Here, atomistic simulations were used to produce Brouwer diagrams from which the solubility of lithium in amorphous structures representing complex grain boundaries have been predicted. The solubility of lithium in these amorphous structures is predicted to be high and will produce an elevated concentration of oxygen defects within the amorphous structure. This could offer a mode for transport of oxygen to the metal oxide interface and, potentially, offer a mechanism or part of a mechanism for observed lithium-accelerated corrosion of Zr-based alloys.

1. Introduction

Nuclear pressurised water reactors (PWRs) use zirconium alloys to clad the fuel, separating the coolant from the fissile fuel. Zirconium alloys are used due their low neutron cross section and adequate corrosion in high temperature aqueous environments of a typical light water reactor (~300°C) [1]. Boron is often added to the coolant water in the form of boric acid, which acts as a shim to control the reactivity of the core [2]. The pH is elevated (at operational temperature to around 7–7.4) to minimise the corrosion of the water-wetted stainless steels and

nickel-based and zirconium alloys. Lithium is added to the coolant chemistry to minimise corrosion by countering the negative effect of boric acid in the form of lithium hydroxide (LiOH). This is to obtain an elevated pH with ~2 ppm Li (as LiOH) for a pH of 10 at room temperature without Boric acid, normal guidelines restrict upper Li concentrations to 3.5, and even 5 ppm for some plant operations, for early cycle high B content, which means the pH is slightly lower early in each operational cycle [3].

Boron combined with lithium has been found within crud deposits on the fuel cladding [4]. These deposits can induce axial offset anomalies in

* Corresponding author.

E-mail address: g.stephens@bangor.ac.uk (G.F. Stephens).

<https://doi.org/10.1016/j.jnucmat.2023.154780>

Received 3 August 2023; Received in revised form 17 September 2023; Accepted 11 October 2023

Available online 13 October 2023

0022-3115/© 2023 The Authors. Published by Elsevier B.V. This is an open access article under the CC BY-NC-ND license (<http://creativecommons.org/licenses/by-nc-nd/4.0/>).

the neutron flux which have been shown to reduce the overall efficiency of electricity generation by up to 70% during the course of several months due to end of cycle shutdown margins from a reduction in available capacity [5,6]. To combat this, new small modular reactor (SMR) designs aim to remove this phenomenon by operating soluble boron-free primary circuits, relying on control-rods alone to control the reactor [7]. Despite this, radiolysis effects would persist and the pH balance within the coolant water would still need to be controlled, hence the continued interest in the use of Li in the primary circuit [8].

Previous investigations have identified that, in the absence of boron, lithium can accelerate the corrosion of zirconium alloys [9–17]. The mechanism for this has yet to be fully understood [11]. A number of hypotheses have been considered in the past, such as electronic aspects, including the change of redox potential in the coolant or enhanced water conductivity through impurities [18]. Volumetric changes of grains or pore growth may contribute to oxygen availability to the metal/oxide interface [17,19]. Recent studies have, however, narrowed the potential mechanisms, noting for example the significant low solubility of Li in bulk ZrO_2 (1.94 eV monoclinic and 2.2 eV tetragonal) [20]. Experimental evidence of Li enrichment along grain boundaries has been observed [21] using atom probe tomography.

The oxide that forms on zirconium alloys consists of two main polymorphs: tetragonal and monoclinic. The tetragonal polymorph is found in higher concentrations at the surface and the metal-oxide interface [22] and is stabilised by compression and small grain sizes [23]. This polymorph was once suggested to offer partial protection from corrosion in normal conditions. It is, however, highly soluble in high-temperature water [24] and studies with ZIRLO, which produces a significantly thinner tetragonal layer that is more corrosion resistant than Zircaloy [25]. This indicates that an alternative mechanism is involved in which the tetragonal layer is not protective. The tetragonal-rich layer grows into the metal and maintains a relatively constant thickness as individual oxide grains grow or experience stress relief and transform to the monoclinic polymorph. Most of the monoclinic part of the oxide contains a high density of cracks and nanopores [26,27]. Where these are interconnected and connect to the surface, the predominantly monoclinic layer is unprotective [24]. A third structure can also be considered: the grain boundaries. [28]. Grain boundaries can be considered low-angle or high-angle. Low angle boundaries have a clear, orderly structure which can be related back to the lattice structure of the grains, but high angle boundaries are more difficult to describe. They may show short range order or some repetition in their structures, but they have much in common with amorphous structures. Evidence shows that highly complex grain boundaries are expected to form in oxides [28]. Migration along grain boundaries in some oxides is expected to be more rapid than through the bulk, [29]. Also, diffusion rates are significantly higher than the bulk, in agreement with experimental assessments of complexity in grain boundaries [30–33].

After noting that the solubility of Li is low in the monoclinic and tetragonal polymorph bulk crystals [20] it is prudent to assess the solubility of Li at the complex grain boundary structures that may exist within PWR zirconium oxides, and to assess the mechanism by which Li is accommodated. The present investigation uses amorphous zirconia as an analogue to the complex grain boundary structures (similar to previous work in ZrO_2 [29] and UO_2 [34]). It then employs atomic scale modelling, combining classical molecular dynamics, reverse Monte-Carlo and density functional theory, to produce Brouwer diagrams that predict defect concentrations and complexes within the amorphous phase. This allowed solution energies to be predicted and compared against the crystalline solution energies to show whether Li is likely to segregate to amorphous grain boundary regions. Volume changes resulting from lithium incorporation into the amorphous structures were also calculated.

2. Method

Creating a simulated amorphous structure which could then be used to assess defect formation energies and predictive defect concentrations required several steps. The method used within this investigation followed previous work [35] where molecular dynamics was first used to melt and quench a relatively large number of atoms from a crystal structure into an amorphous structure. To reduce the size of the resulting structure and enable a less computationally expensive number of atoms for further study, reverse Monte-Carlo was used which can retain a representative distribution of atoms at a much smaller scale. With the smaller structures obtained, the defect formation energies could then be calculated using density functional theory along with electronic structure calculations. This method has been shown to produce representative zirconia amorphous structures using empirical potentials and comparable to experimental results [36]. These could then be used to create Brouwer diagrams which provide an indication of expected defect concentrations in the amorphous structures.

2.1. Molecular Dynamics

The amorphous structure was created using classical molecular dynamics with the LAMMPS package [37] with a supercell of 6144 atoms of cubic ZrO_2 with 2048 formula units in an $8 \times 8 \times 8$ structure in a similar manner to previous work [29]. The structure was heated gradually from 300 to 5000 K in the isothermal-isobaric thermodynamic ensemble (NPT) with a heating rate of 10 K/ps followed by a 10 ps equilibration in the liquid state. The melt was then cooled to room temperature (300 K) using a cooling rate of 2.35 K/ps to produce a quenched amorphous structure [29,36]. The obtained amorphous structure was further relaxed at 300K for 1000 ps. The Cooper-Rushton-Grimes (CRG) model was used for the multi-body pair potentials to account for atomic interactions [38,39]. The isothermal-isobaric thermodynamic ensemble (NPT) used the Nosé-Hoover thermostat and barostat [40]. Constant volume calculations are required when producing Brouwer diagrams as this sets a limit in defect dilution [41,42]. The structure containing 6144 atoms is comprised of 64 supercell structures containing 96 atoms each that could individually be used in density functional theory calculations. To alter the stoichiometry in a manner that can be tractably handled with integer numbers of atoms in the density functional theory calculations (after the reverse Monte Carlo scheme described subsequently), vacant oxygen and vacant zirconium sites were added to the MD stage, removing 64 oxygen atoms for one structure and 64 zirconium atoms for another from the, 6144 atom supercell. This would produce a single vacancy in the reduced structure ready for density functional theory. Similarly for interstitials, 64 oxygen and 64 zirconium atoms were also added to the 6144 atom structure to produce the oxygen and zirconium interstitials that results in a single interstitial specie after the Monte Carlo supercell reduction. These were calculated at constant volume to test whether this would have any bearing on the eventual defect concentrations when producing the Brouwer diagrams. This could then be compared with a standard amorphous structure at constant pressure and a freedom of volumetric movement during the MD calculations, reducing the structure using Reverse Monte Carlo (RMC), and then introducing defects with constant volume calculations using density functional theory.

2.2. Reverse Monte-Carlo

Reverse Monte Carlo was used to reduce the structure size from 6144 to a $2 \times 2 \times 2$ supercell of 96 atoms containing 32 formula units of ZrO_2 that could then be readily computed using density functional theory calculations in a computationally tractable manner. This is to reduce the number of atoms in the structure to enable density functional theory calculations which are much more computationally expensive. The

purpose of using RMC is to avoid possible crystallisation in small cells [36]. In order to achieve this, a method had previously been devised to maintain Zr-O, O-O and Zr-Zr partial pair correlations using RMC [36]. To confirm that the remaining structure maintained the radial distribution function (RDF) after RMC, the RDF prior and post RMC were compared and found to be in good agreement and was repeated 10 times to ensure consistent results. RDF confirmation was made after each subsequent DFT calculation to ensure the structure remained amorphous. Fig. 1 shows a particular structure that has been reduced to 96 atoms using RMC and has also undergone a DFT relaxation under constant volume along with the addition of a lithium interstitial (blue).

2.3. Density functional theory (DFT)

The Vienna Ab initio simulation package (VASP) was used for DFT calculations with project augmented wave pseudopotentials (PAW) [43–46]. The Perdew-Burke-Ernzerhof (PBE functional) was used with a cut-off energy of 500 eV. Plane wave simulations were conducted with a quasi-Newton algorithm to relax ions into their instantaneous ground state. The atomic force threshold criteria were set to 10^{-3} eV/Å with the electronic relaxation criterion set to 1×10^{-4} eV. The structure was first relaxed with constant pressure calculations before constant volume calculations could be made, as required for Brouwer diagram calculations [38]. At each stage, RDF calculations were made to ensure the structure remained amorphous. Defects could then be added where all structures were first calculated with a $2 \times 2 \times 2$ k-point mesh, which was then increased to a $4 \times 4 \times 4$ k-point mesh to increase accuracy. Charged defects were calculated by adding or subtracting electrons to the supercell which were allowed to relax to a preferable position whilst maintaining an overall negative or positive charge, respectively. To maintain consistency with previous bulk work [20], the k-point mesh was set as Monkhorst-pack with increased accuracy due to an increase in sampling points. Each defect was positioned in 10 separate locations at random within the amorphous structure to gain both a range of values and to find the averages.

2.4. Brouwer Diagram and Formation Energy of Charged Defects

Brouwer diagrams provide an indication of defect concentration against the partial pressure of oxygen, which can be considered analogous to the distance from the oxide-water interface in an oxide scale within a material. The value of partial pressure at the water-oxide interface was previously estimated to be $10^{-5.46}$ atm, or 10.1325 Pa, at 635 K and [20], a typical temperature for reactor operation [20].

The formation energy graph is used to predict defect formation energies as a function of the Fermi level change (Given in Fermi energy) across the bandgap. The lower the formation energy of a defect species, the more likely that the defect will feature on the Brouwer diagram with higher concentrations. The Brouwer diagrams present predicted defect

concentrations throughout a semiconducting material whilst maintaining charge neutrality.

The Fermi energy vs formation energy graphs and Brouwer diagrams were calculated using the DefAp 2.7 script which also required the electronic properties of the structure that were available from the DFT calculations [20]. The defects considered had a range of charges from neutral to ± 4 and included interstitials (over-coordinated), vacancies (under-coordinated), substitutions, and small clusters of defects. The defects are described in Kröger-Vink notation [47] where the superscript \times indicates a relatively neutral charge on the defect i.e., the site is associated with the same charge state whether it is occupied as in the perfect crystal or by a defect. \bullet indicates that the defect site is more positively charged than in the perfect crystal, and $'$ a relatively negative charge. Interstitials were thus (O_i^\times) (O_i^\bullet) (O_i') , (Zr_i^\times) (Zr_i^\bullet) (Zr_i') $(Zr_i^{\bullet\bullet})$ $(Zr_i^{\bullet\bullet\bullet})$ $(Zr_i^{\bullet\bullet\bullet\bullet})$, (Li_i^\times) (Li_i^\bullet) ; Vacancies were (V_O^\times) (V_O^\bullet) (V_O') , (V_{Zr}^\times) (V_{Zr}^\bullet) (V_{Zr}') $(V_{Zr}^{\bullet\bullet})$ $(V_{Zr}^{\bullet\bullet\bullet})$. The substitutions (Li_O) and (Li_{Zr}) were reviewed but were not found during Brouwer diagram calculations with the exception of the small cluster of 2 lithium atoms around a vacant zirconium site $\{2Li;V_{Zr}\}$. For each Brouwer diagram, the maximum DFT energy values were used to make one calculation and then again with minimum over all defect location changes. These two calculations were combined to produce a range of values of defect concentration per unit formula ZrO_2 .

2.5. Lithium Solubility in Amorphous ZrO_2

Lithium solubility could be ascertained by attempting chemical reaction equations using the DFT energies and comparing reactant and product energies. A positive value would represent an endothermic reaction, indicating low possibility of solubility, and a negative value would represent an exothermic reaction and indicate possible solubility [48].

3. Results

3.1. Producing Amorphous ZrO_2

To confirm that the structures produced after the molecular dynamics melt/quench process and that the smaller structures that were subsequently produced by reverse Monte-Carlo for density functional theory were amorphous, radial distribution function (RDF) calculations were made for both the LAMMPS structure and the final VASP structures to ensure that no long-range order was observed after the conversion into the smaller system using reverse Monte-Carlo.

Ten molecular dynamic calculations were conducted and were checked for radial distribution to ensure that the amorphous structures were consistent with previous works [29] and that any deviations in distribution were minimal without any sign of crystallisation. Fig. 2 shows typical RDF distributions from these calculations, highlighting

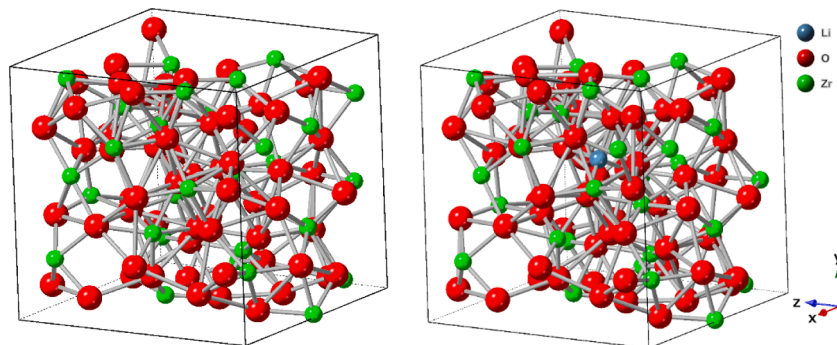


Fig. 1. Amorphous $2 \times 2 \times 2$ ZrO_2 supercell post Reverse Monte-Carlo and post DFT relaxation with a) a standard amorphous structure and b) lithium interstitial (blue).

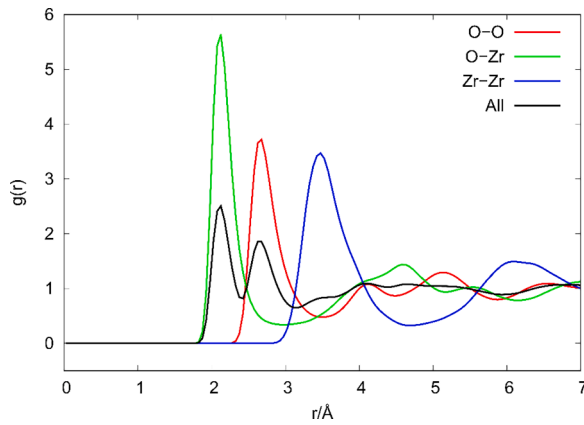


Fig. 2. A range of partial radial distributions ($g(r)$) vs radius ($r/\text{\AA}$) of O-O, O-Zr, Zr-Zr and all atoms.

the good repeatability of the systems.

3.2. Lithium accommodation and defects within the amorphous structure

The concept of defects within a glassy or amorphous system is not new [30]. As local order is observed in these systems [49–51], structural vacancies and interstitial species are readily identified from the overall energy of the system and although not associated with a lattice. For ease of communication in this work, they shall be generally referred to as vacancies and interstitial species and their topology is explained where appropriate.

The defects under consideration for the Brouwer diagrams must fit within the bandgap of the defect free semiconductor oxide. The lowest formation energies (i.e., most stable) of these defects will feature on the Brouwer diagram with greater concentrations. The bandgap was calculated ten times from the density of states (DOS) within VASP with an average of $2.78 \text{ eV} \pm 0.26$. Whilst experimental measurements of the bandgap vary greatly for amorphous ZrO_2 (Range from 3.7 and 6.12 eV) which has been attributed to density changes and defects within the amorphous structures [52,53]. Photoluminescence has identified a bandgap of 2.8 eV, which is representative of the value gained during simulations [53–55]. Fig. 3 reports the formation energies of the most stable defects as a function of bandgap Fermi level. All other defects were not found within the Brouwer diagram calculations by either having a higher formation energy or were calculated outside of the Fermi energy range.

Fig. 3 reports that the -2 charged vacant zirconium site ($V_{\text{Zr}}^{''}$) and the small cluster of 2 +1 lithium interstitials around a ($V_{\text{Zr}}^{''}$) vacant

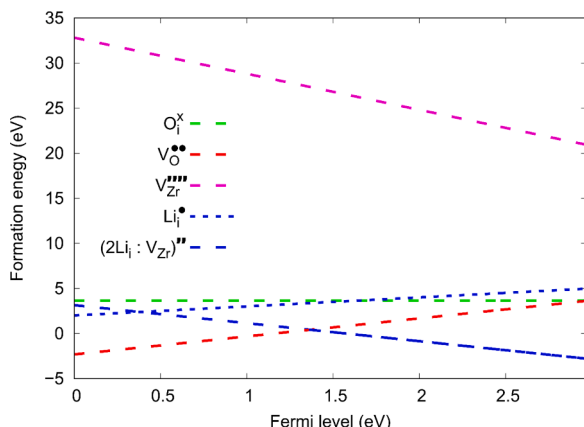


Fig. 3. Average formation energy for each defect type across the bandgap.

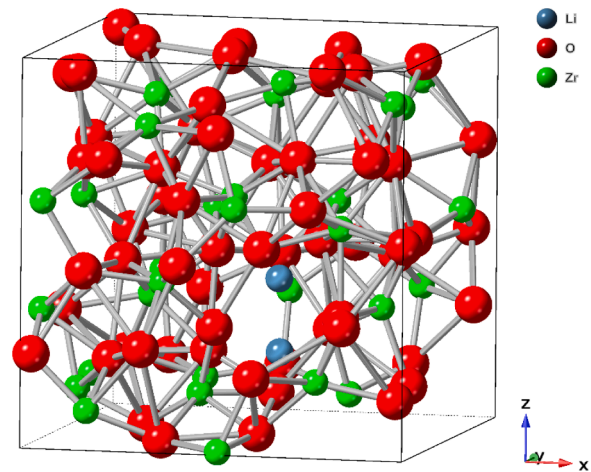


Fig. 4. 2 Li atoms around a vacant Zr location.

zirconium site $\{2\text{Li}_i : V_{\text{Zr}}^{''}\}^{\bullet\bullet}$ (structure in Fig. 4) share the lowest formation energy across the bandgap. The double positive charged vacant oxygen defects show the lowest formation energy towards the valence band (0 eV) where the double negative charged anion cluster, $\{2\text{Li}_i : V_{\text{Zr}}^{''}\}^{\bullet\bullet}$, shows a lower formation energy towards the conduction band (2.96 eV). This provides an indication that the aforementioned defects will feature heavily in the Brouwer diagrams. Vacant oxygen defects are expected to be prevalent where electron concentrations are higher than the hole concentration, and that the small cluster will be more prevalent where hole concentrations are higher, and enough Li is present.

Interestingly, the -4 charged vacant zirconium ($V_{\text{Zr}}^{''''}$) is predicted to form with a high formation energy across the bandgap. This is unlike the previously published results assessing behaviour in crystalline monoclinic and tetragonal systems [20], so the ($V_{\text{Zr}}^{''''}$) defect is expected to be less prevalent in the amorphous structure. When comparing these defect formation results with previous work, [20], where deviation in stoichiometry are found to be more likely in amorphous structures than that of crystalline ZrO_2 , we have found that the formation energy of O_i to be lower than the energies previously reported for the bulk crystalline structures (5.23 eV in bulk and 3.67 eV in amorphous) [20]. In Fig. 3, the formation energy is $< 5 \text{ eV}$ across the bandgap. A O-O bond distance of 1.43 \AA was observed with the introduction of an oxygen interstitial which has been previously reported as a predicted peroxide [36]. It was hypothesised that the peroxide might be a route for oxidation along the grain boundaries.

As the Li containing cluster is an extrinsic defect, the concentration of this and other Li containing defect clusters was specified in order to assess concentration dependent behaviour. By altering the lithium concentration, this can provide an indication of the increase or decrease of intrinsic defects as a result of the lithium's inclusion within the structure. The Brouwer diagram shows defect concentrations on the y-axis and the partial pressure of oxygen, P_{O_2} on the x-axis. The P_{O_2} associated with the water-oxide interface at 635 K is shown by the vertical line. The lithium concentration is altered from 10^{-1} in Fig. 5 a, and then reduced through 10^{-5} , 10^{-11} and finally to zero lithium in Fig. 5 b, c, and d, respectively. Ten calculations were conducted with the maximum and minimum values are shown with a range given in a shaded area. The concentration of Li locally within the grain boundary may be significantly higher than the overall bulk concentration. Experimental work has shown lithium segregation along grain boundaries [21].

When calculating the solution energies of lithium into the zirconia structures, it was previously identified that lithium was unlikely to form a solution with the bulk ZrO_2 . However, when comparing this with the

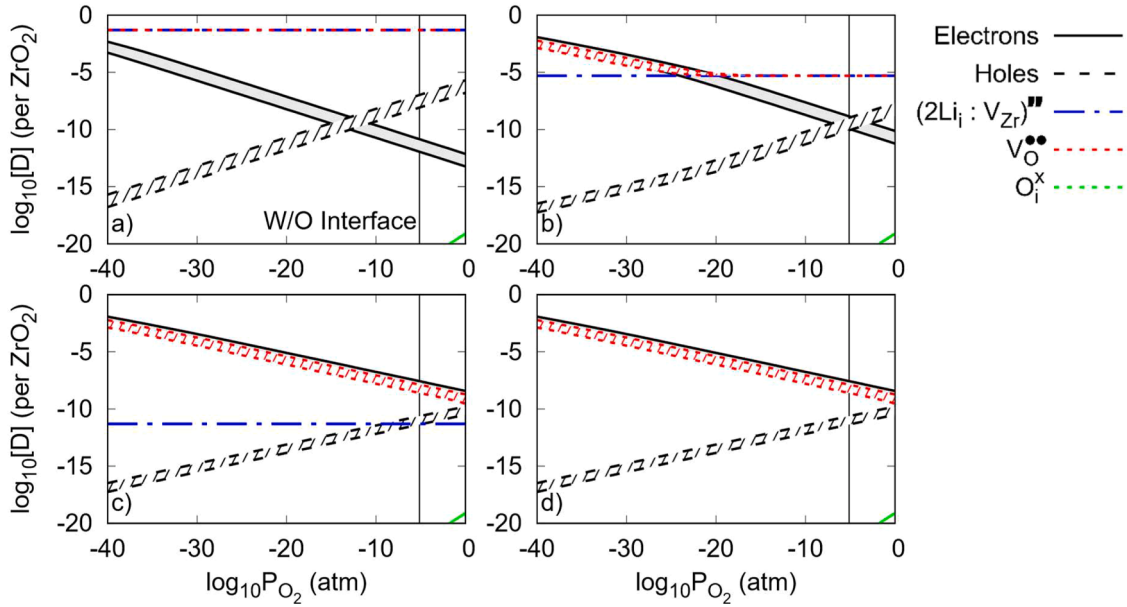
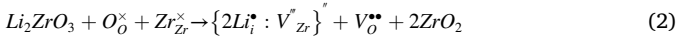
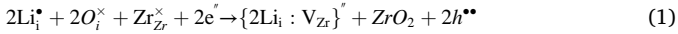


Fig. 5. 635 K amorphous ZrO_2 Brouwer diagrams with defect concentrations [D] per unit amorphous ZrO_2 for (a) 10^{-1} Li (b) 10^{-5} Li (c) 10^{-11} Li and (d) no Li with only intrinsic defects. The black solid line represents electron concentrations, black dashed is holes, blue dashed is $\{2\text{Li}_i : \text{V}_{\text{Zr}}\}'''$, red dashed is $(\text{V}_{\text{O}}^{\bullet\bullet})$, and the green solid line at the bottom right is (O_i^x) . The vertical black line to the right of the diagrams represents the calculated water oxide interface [20]. Shaded areas represent the minimum to maximum values calculated for each defect.

amorphous structure, a possible solution energy can be considered:



The reaction equation above (1) assesses whether the lithium interstitial is more stable than the lithium cluster. The energy difference was found to be between 3.0 to 3.2 eV depending on defect location. This indicates that the small lithium cluster is more likely to form solution than the isolated lithium interstitial. Assessing the lithium solution into the structure via equation (2) produces an average solution energy of -0.38 eV (with a standard deviation of 1.27 eV), highlighting a significant portion of the considered clusters are soluble within the structure. This behaviour is similar to the deviation in oxygen stoichiometry in UO_2 observed, whereby a range of solution energies were predicted, including a significant portion of negative solution energies [56]. This solution mechanisms also increases the number of vacant oxygen defects within the structure as is reported in the Brouwer diagrams (see Fig. 5).

Previous works within literature showed, after 195 days exposure to water containing 250 wt. ppm Li, atom probe had identified a concentration of 0.0013 ± 0.001 at. % Li averaged across the sample. Furthermore, the lithium segregation along the grain boundaries produced between 0.2 to 0.6 at. % Li concentrations [57]. For this reason, a range of Li concentrations were reviewed. The study also identified the lithium segregation grain boundary width to be between 1 and 1.5 nm. The Li found along grain boundaries provide an indication of complexation, but further work would need to be undertaken to identify the level of complexation. Previous work has identified the grain boundary complexity in chromium doped UO_2 where similar techniques may be employed [58]. Other work has also showed that the number of non-CSL grain boundaries dominates most ceramics [59].

When comparing the concentrations in Fig. 5, the highest lithium concentration of 10^{-1} (a) shows a large increase in $(\text{V}_{\text{O}}^{\bullet\bullet})$ per ZrO_2 when compared to the zero Li figure (d), particularly at the water/oxide interface. In addition to this, the electron and hole convergence is brought to the water/oxide interface, which would usually be a position of equal ratio for anionic and cationic defects. As the lithium

concentrations are reduced, the impact on intrinsic defects is reduced. This might explain experimental work which shows that only higher Li concentrations within coolant water will accelerate the corrosion rate [15,17].

4. Discussion

Creating the amorphous structures for simulation provided two methods which had the potential to provide two different results. On one hand, the defects were produced during the molecular dynamics stage where under-coordinated, over-coordinated or extrinsic defect structures containing around 8000 atoms could be produced. All structures required an equal volume to that of the stoichiometric structure to ensure that a limit of defect dilution could be provided, which is the case when producing Brouwer diagrams. These defects could then be reduced through Monte-Carlo to around 100 atoms and the relaxed energy for the structure through DFT calculations, continuing with constant volume, could be gained for Brouwer diagram calculations. On the other hand, the stoichiometric amorphous structure could be produced via molecular dynamics, reduced through Monte-Carlo and then have the defects applied at the DFT calculations stage. Whilst the later reduced the number of steps required in molecular dynamics and Monte-Carlo calculations reducing computational time overall, the argument could be made that, in particular, the properties of an under-coordinated or over-coordinated amorphous structure could be different. For this reason, both methods were conducted and, in the case of Brouwer diagram calculations, the results were similar enough to be considered negligibly different and did not alter the final outcome. Whilst this might be the case for amorphous ZrO_2 , that is not to say that it is something which could be deemed the norm for all cases and care should be taken with any future work using a similar method. Whilst more computationally expensive, the first method is expected to produce the most reliable results, but no such study is known to have taken place to verify this.

Changing the location of a defect within the amorphous structure has been found to slightly alter the defect concentrations that can be expected when presented in Brouwer diagrams. This does not only alter the concentration of the defect in question, but also has a knock-on effect of

other defects, including the electron and hole concentrations. The only exception to this is where the defect species has a stipulated concentration, such as lithium used in this investigation.

Whilst creating Brouwer diagrams require a solution limit of defects by maintaining a constant volume throughout all calculations, each defect would produce an increase or decrease in pressure as a result. These pressures range from -46.3 kbar in the case of the plus two charged vacant oxygen ($V_O^{\bullet\bullet}$) and 31.08 kbar in the negative four charged vacant zirconium ($V_{Zr}^{\bullet\bullet}$). For the small lithium cluster ($2Li : V_O$) there is a pressure increase of 23.9 kbar. These pressure changes are high in relation to each defect and present a possible limitation to the method, but is inevitable given the relatively small size of the supercells that are computationally viable. Defects such as the plus two charged vacant oxygen have, however, been identified within yttria-doped ZrO_2 samples up to 10 kbar experimentally [60] and, although a reduction in vacant oxygen defects were found, up to 149 kbar through simulation [61]. That being said, this is likely an area that would require further study to verify or provide an indication of possible deviation in predictions from empirically obtained data.

The Brouwer diagrams indicate that lithium increases the vacant oxygen concentration, particularly at the water/oxide interface. Whilst current experimental evidence has shown that lithium does segregate along the complex grain boundaries [21], further experimental work will need to be conducted to confirm the increase of vacant oxygen concentration and validate these simulated results. This would provide a solid foundation to underpin the mechanisms by which lithium accelerates the corrosion of zirconium alloys and provide a base in which to investigate methods in which to mitigate this. Solutions may include alloying additions that may suppress the elevation of vacant oxygen concentrations or alternative alkaline coolant additives which may prevent the increase in vacant oxygen also. Both of these potential routes of investigation could use similar methods shown in this work to identify targeted experiments for validation and provide a solution to the lithium accelerated corrosion issue.

5. Conclusion

A combination of molecular dynamics, reverse Monte-Carlo, and density functional theory have been used to investigate the observed phenomenon of accelerated corrosion of Zr-based cladding in a pressurised water reactor coolant containing Li. The role and stability of Li at amorphous grain boundaries in the ZrO_2 structure have been investigated. The structure was determined and compared to previous modelling work using radial distribution function analysis.

Brouwer diagrams have shown that, if amorphous zirconia can be used as an analogue for high-angle grain boundaries, then an increase in the grain boundary lithium concentration will induce greater concentrations of under-coordinated cation sites in the boundary (for ease referred to as vacant oxygen sites). Previous work has shown that vacant oxygen defects can become a source of oxygen transport in crystalline and amorphous systems [29,31–33].

Li has been calculated to be soluble in the amorphous structure with respect to the Li_2ZrO_3 compound, using the results from the Brouwer diagram to inform the solution mechanism. The same method that found solubility in the bulk to be low was utilized [20]. The solution energy of -0.38 eV with a standard deviation of 1.27 means that the solubility is largely temperature independent, however this does not consider kinetic effects related to Li ingress. The increase in oxygen vacancy concentration within the amorphous phase may account for an accelerated corrosion rate within environments with higher lithium concentrations and further work to assess the impact of the Li solution on kinetics is underway.

We can conclude that Li accommodation along disordered grain boundaries is mechanistically viable and corroborates with experimental observations [21].

CRedit authorship contribution statement

Gareth F. Stephens: Conceptualization, Formal analysis, Investigation, Writing – original draft, Visualization. **Megan W. Owen:** Methodology, Writing – review & editing. **El Mehdi Ghardi:** Software, Writing – review & editing. **Alberto Fraile:** Methodology, Writing – review & editing. **Susan Ortner:** Validation, Writing – review & editing. **Michael J.D. Rushton:** Methodology, Software, Validation. **William E. Lee:** Resources, Supervision, Funding acquisition. **Aidan Cole-Baker:** Validation, Resources, Writing – review & editing, Supervision, Funding acquisition. **Simon C. Middleburgh:** Conceptualization, Methodology, Validation, Resources, Writing – review & editing, Supervision, Project administration, Funding acquisition.

Declaration of Competing Interest

The authors declare the following financial interests/personal relationships which may be considered as potential competing interests: Gareth F Stephens reports financial support was provided by Engineering and Physical Sciences Research Council. Gareth F Stephens reports financial support was provided by Jacobs UK Limited London.

Data availability

Data will be made available on request.

Acknowledgements

All calculations in this study were performed on Supercomputing Wales. SCM, MJDR and WEL are funded through the Sêr Cymru II programme by Welsh European Funding Office (WEFO) under the European Development Fund (ERDF). GFS is funded through the Nuclear Energy Futures Centre for Doctoral Training (EP/S023844/1), co-sponsored by Jacobs Engineering Group. This work is associated with the MIDAS (Mechanistic Understanding of Irradiation Damage in Fuel Assemblies) forum.

References

- [1] L. Hallstadius, S. Johnson, E. Lahoda, Cladding for high performance fuel, *Progress in Nuclear Energy* 57 (2012) 71–76, <https://doi.org/10.1016/j.pnucene.2011.10.008>.
- [2] Y.A. Hassan, S. Osturk, S. Lee, Rheological characterization of buffered boric acid aqueous solutions in light water reactors, *Progress in Nuclear Energy* 85 (2015) 239–253, <https://doi.org/10.1016/j.pnucene.2015.06.025>.
- [3] F. Nordmann, PWR and BWR chemistry optimization, 56, *Nuclear Engineering International*, 2011, p. 24. <https://www.neimagazine.com/features/featurepwr-and-bwr-chemistry-optimization/>, accessed July 27, 2023.
- [4] I.D. Dobrevski, K.F. Minkova, R.A. Ivanova, Possible impact on the occurrence of axial offset anomaly, *Power Plant Chemistry* 5 (4) (2018) 197–202.
- [5] P.L. Frattini, J. Blok, S. Chauffriat, J. Sawicki, J. Riddle, Axial offset anomaly: Coupling PWR primary chemistry with core design, *Nuclear Energy* 40 (2001) 123–135.
- [6] J. Blok, S. Chauffriat, P. Frattini, Modeling the axial offset anomaly in PWRs, in: *Proceedings of International Conference on Water Chemistry of Nuclear Reactor Systems—Operation Optimisation and New Developments*, 2002, pp. 1–9.
- [7] P.P. Sanchez, A. dos Santos, Prediction of the Power Peaking Factor in a Boron-Free Small Modular Reactor Based on a Support Vector Regression Model and Control Rod Bank Positions, *Nuclear Science and Engineering* 195 (2021) 555–562, <https://doi.org/10.1080/00295639.2020.1854541>.
- [8] J. Mart, A. Klein, A. Soldatov, Feasibility study of a soluble boron-free small modular integral pressurized water reactor, *Nucl Technol* 188 (2014) 8–19, <https://doi.org/10.13182/NT13-135>.
- [9] D. Pêcheur, J. Godlewski, J. Peybernès, L. Fayette, M. Noé, A. Frichet, O. Kerrec, Contribution to the understanding of the effect of the water chemistry on the oxidation kinetics of Zircaloy-4 cladding, *ASTM Special Technical Publication*, 2000, <https://doi.org/10.1520/stp14328s>.
- [10] B.A. Murgatroyd, J. Winton, Hydriding Zircaloy-2 in lithium hydroxide solutions, *Journal of Nuclear Materials* 23 (1967) 249–256, [https://doi.org/10.1016/0022-3115\(67\)90157-2](https://doi.org/10.1016/0022-3115(67)90157-2).
- [11] N. Ramasubramanian, N. Precoanin, V. Ling, Lithium Uptake and the Accelerated Corrosion of Zirconium Alloys, in: *Zirconium in the Nuclear Industry: Eighth*

- International Symposium, 2008, p. 187, <https://doi.org/10.1520/stp18865s>. -187–15.
- [12] D. Pêcheur, J. Godlewski, P. Billot, J. Thomazet, Microstructure of Oxide Films Formed during the Waterside Corrosion of the Zircaloy-4 Cladding in Lithiated Environment, in: *Zirconium in the Nuclear Industry: Eleventh International Symposium*, 2009, <https://doi.org/10.1520/stp16169s>.
 - [13] F. Garzaroli, J. Pohlmeier, S. Trap-Pretsching, H.G. Weidinger, *Fundamental Aspects Of Corrosion On Zirconium Base Alloys In Water Reactor Environments Proceedings Of A Technical Committee Meeting Organized By The International Atomic Energy Agency*, in: IAEA Technical Committee Meeting Proceedings, 1990, pp. 65–72.
 - [14] I.L. Bramwell, P.D. Parsons, D.R. Tice, Corrosion of Zircaloy-4 PWR fuel cladding in lithiated and borated water environments, 1991. http://inis.iaea.org/Search/seaarch.aspx?orig_q=RN:23052627, accessed May 2, 2023.
 - [15] Y.H. Jeong, K.H. Kim, J.H. Baek, Cation incorporation into zirconium oxide in LiOH, NaOH, and KOH solutions, *Journal of Nuclear Materials* 275 (1999) 221–224, [https://doi.org/10.1016/S0022-3115\(99\)00148-8](https://doi.org/10.1016/S0022-3115(99)00148-8).
 - [16] A.T. Motta, A. Yilmazbayhan, R.J. Comstock, J. Partezana, G.P. Sabol, B. Lai, Z. Cai, Microstructure and Growth Mechanism of Oxide Layers Formed on Zr Alloys Studied with Micro-Beam Synchrotron Radiation, *J ASTM Int* 2 (2005), <https://doi.org/10.1520/JAI12375>.
 - [17] H. Hulme, A. Panteli, F. Pickering, M. Gass, A. Cole-Baker, P. Binks, M. Fenwick, M. Waters, J. Smith, Investigating the Corrosion Behaviour of Zircaloy-4 in LiOH under a Thermal Gradient and Two-Phase Flow Regime, in: *Zirconium in the Nuclear Industry: 19th International Symposium*, 2021, pp. 537–563, <https://doi.org/10.1520/stp162220190008>.
 - [18] B. Cox, Some thoughts on the mechanisms of in-reactor corrosion of zirconium alloys, *Journal of Nuclear Materials* 336 (2005) 331–368, <https://doi.org/10.1016/J.JNUCMAT.2004.09.029>.
 - [19] J. Yang, M. Youssef, B. Yildiz, Electro-chemo-mechanical effects of lithium incorporation in zirconium oxide, *Phys Rev Mater* 2 (2018), <https://doi.org/10.1103/PhysRevMaterials.2.075405>.
 - [20] G.F. Stephens, Y.R. Than, W. Neilson, L.J. Evitts, M.R. Wenman, S.T. Murphy, R. W. Grimes, A. Cole-Baker, S. Ortnor, N. Gotham, M.J.D. Rushton, W.E. Lee, S. C. Middleburgh, The accommodation of lithium in bulk ZrO₂, *Solid State Ion.* 373 (2021), <https://doi.org/10.1016/j.ssi.2021.115813>.
 - [21] P. Styman, A. Garner, J. Robinson, A. Cole-Baker, S. Ortnor, *Characterising The Effect Of Li On Zircaloy Corrosion*, (In Press) Fontevraud 10, 2022.
 - [22] F. Baxter, A. Garner, M. Topping, H. Hulme, P. Preuss, P. Frankel, Phase stability of zirconium oxide films during focused ion beam milling, *Journal of Nuclear Materials* 504 (2018) 176–180, <https://doi.org/10.1016/j.jnucmat.2018.03.037>.
 - [23] P.G. Frankel, J. Wei, E.M. Francis, A. Forsey, N. Ni, S. Lozano-Perez, A. Ambard, M. Blat-Yrieix, R.J. Comstock, L. Hallstadius, R. Moat, C.R.M. Grovenor, S. Lyon, R. A. Cottis, M. Preuss, Effect of Sn on corrosion mechanisms in advanced Zr-cladding for pressurised water reactors, *ASTM Special Technical Publication*, ASTM International, 2015, pp. 404–437, <https://doi.org/10.1520/STP154320130006>.
 - [24] M. Oskarsson, E. Ahlberg, K. Pettersson, Oxidation of Zircaloy-2 and Zircaloy-4 in water and lithiated water at 360°C, *Journal of Nuclear Materials* (2001), [https://doi.org/10.1016/S0022-3115\(01\)00480-9](https://doi.org/10.1016/S0022-3115(01)00480-9).
 - [25] H. Swan, M.S. Blackmur, J.M. Hyde, A. Laferriere, S.R. Ortnor, P.D. Styman, C. Staines, M. Gass, H. Hulme, A. Cole-Baker, P. Frankel, The measurement of stress and phase fraction distributions in pre and post-transition Zircaloy oxides using nano-beam synchrotron X-ray diffraction, *Journal of Nuclear Materials* 479 (2016) 559–575, <https://doi.org/10.1016/J.JNUCMAT.2016.07.024>.
 - [26] S.S. Yardley, K.L. Moore, N. Ni, J.F. Wei, S. Lyon, M. Preuss, S. Lozano-Perez, C.R. M. Grovenor, An investigation of the oxidation behaviour of zirconium alloys using isotopic tracers and high resolution SIMS, *Journal of Nuclear Materials* 443 (2013) 436–443, <https://doi.org/10.1016/j.jnucmat.2013.07.053>.
 - [27] J. Hu, A. Garner, N. Ni, A. Gholinia, R.J. Nicholls, S. Lozano-Perez, P. Frankel, M. Preuss, C.R.M. Grovenor, Identifying suboxide grains at the metal-oxide interface of a corroded Zr-1.0%Nb alloy using (S)TEM, transmission-EBSD and EELS, *Micron* 69 (2015) 35–42, <https://doi.org/10.1016/j.micron.2014.10.004>.
 - [28] P.R. Cantwell, M. Tang, S.J. Dillon, J. Luo, G.S. Rohrer, M.P. Harmer, Grain boundary complexions, *Acta Mater* 62 (2014) 1–48, <https://doi.org/10.1016/j.actamat.2013.07.037>.
 - [29] M.W. Owen, M.J.D. Rushton, L.J. Evitts, A. Claisse, M. Puide, W.E. Lee, S. C. Middleburgh, Diffusion in doped and undoped amorphous zirconia, *Journal of Nuclear Materials* 555 (2021), 153108, <https://doi.org/10.1016/j.jnucmat.2021.153108>.
 - [30] S.J. Dillon, M.P. Harmer, J. Luo, Grain boundary complexions in ceramics and metals: An overview, *Jom* 61 (2009) 38–44, <https://doi.org/10.1007/s11837-009-0179-3>.
 - [31] M. Jublot, G. Zumpicchiati, M. Tupin, S. Pascal, C. Berdin, C. Bisor, M. Blat-Yrieix, Influence of hydride precipitation on the corrosion kinetics of zircaloy-4: Effect of the nanostructure and grain boundary properties of the zirconium oxide layer on oxygen diffusion flux, *ASTM Special Technical Publication*, ASTM International, 2018, pp. 350–384, <https://doi.org/10.1520/STP159720160073>.
 - [32] A.D. Le Claire, The analysis of grain boundary diffusion measurements, 1963, <https://doi.org/10.1088/0508-3443/14/6/317>.
 - [33] X. Guo, Low temperature degradation mechanism of tetragonal zirconia ceramics in water: role of oxygen vacancies, *Solid State Ion* 112 (1998) 113–116, [https://doi.org/10.1016/S0167-2738\(98\)00212-4](https://doi.org/10.1016/S0167-2738(98)00212-4).
 - [34] S.C. Middleburgh, W.E. Lee, M.J.D. Rushton, Structure and properties of amorphous uranium dioxide, *Acta Mater* 202 (2021), <https://doi.org/10.1016/j.actamat.2020.10.069>.
 - [35] D. Muñoz Ramo, A. Chronos, M.J.D. Rushton, P.D. Bristowe, Effect of trivalent dopants on local coordination and electronic structure in crystalline and amorphous ZnO, *Thin Solid Films* 555 (2014) 117–121, <https://doi.org/10.1016/j.tsf.2013.05.140>.
 - [36] M.J.D. Rushton, I. Ipatova, L.J. Evitts, W.E. Lee, S.C. Middleburgh, Stoichiometry deviation in amorphous zirconium dioxide, *RSC Adv.* 9 (2019) 16320–16327, <https://doi.org/10.1039/c9ra01865d>.
 - [37] A.P. Thompson, H.M. Aktulga, R. Berger, D.S. Bolintineanu, W.M. Brown, P. S. Crozier, P.J. in 't Veld, A. Kohlmeyer, S.G. Moore, T.D. Nguyen, R. Shan, M. J. Stevens, J. Tranchida, C. Trott, S.J. Plimpton, LAMMPS - a flexible simulation tool for particle-based materials modeling at the atomic, meso, and continuum scales, *Comput Phys Commun* 271 (2022), 108171, <https://doi.org/10.1016/j.cpc.2021.108171>.
 - [38] M.W.D. Cooper, M.J.D. Rushton, R.W. Grimes, A many-body potential approach to modelling the thermomechanical properties of actinide oxides, *Journal of Physics Condensed Matter* 26 (2014), <https://doi.org/10.1088/0953-8984/26/10/105401>.
 - [39] D.G. Frost, C.O.T. Galvin, M.W.D. Cooper, E.G. Obbard, P.A. Burr, Thermophysical properties of urania-zirconia (U,Zr)O₂ mixed oxides by molecular dynamics, *Journal of Nuclear Materials* 528 (2020), <https://doi.org/10.1016/J.JNUCMAT.2019.151876>.
 - [40] M.J.D. Rushton, A. Chronos, Impact of uniaxial strain and doping on oxygen diffusion in CeO₂, *Sci Rep.* 4 (2014) 2–7, <https://doi.org/10.1038/srep06068>.
 - [41] M. Youssef, B. Yildiz, Intrinsic point-defect equilibria in tetragonal ZrO₂: Density functional theory analysis with finite-temperature effects, *Phys Rev B Condens Matter Mater Phys* 86 (2012), <https://doi.org/10.1103/PhysRevB.86.144109>.
 - [42] S.T. Murphy, N.D.M. Hine, Point defects and non-stoichiometry in Li₂TiO₃, *Chemistry of Materials* 26 (2014) 1629–1638, <https://doi.org/10.1021/cm4038473>.
 - [43] G. Kresse, J. Furthmüller, J. Hafner, Theory of the crystal structures of selenium and tellurium: The effect of generalized-gradient corrections to the local-density approximation, *Phys Rev B* 50 (1994) 13181–13185, <https://doi.org/10.1103/PhysRevB.50.13181>.
 - [44] G. Kresse, J. Furthmüller, Efficiency of ab-initio total energy calculations for metals and semiconductors using a plane-wave basis set, *Comput Mater Sci* 6 (1996) 15–50, [https://doi.org/10.1016/0927-0256\(96\)00008-0](https://doi.org/10.1016/0927-0256(96)00008-0).
 - [45] G. Kresse, J. Furthmüller, Efficient iterative schemes for ab initio total-energy calculations using a plane-wave basis set, *Phys Rev B Condens Matter Mater Phys* 54 (1996) 11169–11186, <https://doi.org/10.1103/PhysRevB.54.11169>.
 - [46] D. Joubert, From ultrasoft pseudopotentials to the projector augmented-wave method, *Phys Rev B Condens Matter Mater Phys* 59 (1999) 1758–1775, <https://doi.org/10.1103/PhysRevB.59.1758>.
 - [47] U. Guth, Kröger-Vinks Notation of Point Defects. *Encyclopedia of Applied Electrochemistry*, 2014, https://doi.org/10.1007/978-1-4419-6996-5_310.
 - [48] L. Pilote, A.E. Gheribi, P. Chartrand, Study of the solubility of Pb, Bi and Sn in aluminum by mixed CALPHAD/DFT methods: Applicability to aluminum machining alloys, *CALPHAD*. 61 (2018) 275–287, <https://doi.org/10.1016/j.calphad.2018.04.007>.
 - [49] J. Luo, Stabilization of nanoscale quasi-liquid interfacial films in inorganic materials: A review and critical assessment, *Critical Reviews in Solid State and Materials Sciences* 32 (2007) 67–109, <https://doi.org/10.1080/10408430701364388>.
 - [50] S.J. Dillon, M.P. Harmer, Relating grain-boundary complexion to grain-boundary kinetics I: Calcia-doped alumina, *Journal of the American Ceramic Society* 91 (2008) 2304–2313, <https://doi.org/10.1111/j.1551-2916.2008.02454.x>.
 - [51] S.J. Dillon, M.P. Harmer, Relating grain-boundary complexion to grain-boundary kinetics II: Silica-doped alumina, *Journal of the American Ceramic Society* 91 (2008) 2314–2320, <https://doi.org/10.1111/j.1551-2916.2008.02432.x>.
 - [52] S.M. Chang, R.A. Doong, Interband transitions in sol-gel-derived ZrO₂ films under different calcination conditions, *Chemistry of Materials* 19 (2007) 4804–4810, <https://doi.org/10.1021/cm070606n>.
 - [53] V. Gritsenko, D. Gritsenko, S. Shaimeev, V. Aliev, K. Nasyrov, S. Erenburg, V. Tapilin, H. Wong, M.C. Poon, J.H. Lee, J.W. Lee, C.W. Kim, Atomic and electronic structures of amorphous ZrO₂ and HfO₂ films, *Microelectron Eng* 81 (2005) 524–529, <https://doi.org/10.1016/j.mee.2005.03.056>.
 - [54] T. Ito, M. Maeda, K. Nakamura, H. Kato, Y. Ohki, Similarities in photoluminescence in hafnia and zirconia induced by ultraviolet photons, *J Appl Phys* 97 (2005), <https://doi.org/10.1063/1.1856220>.
 - [55] D. Ciuparu, G. Ensuque, F. Shafeev, Bozon-Verduraz, Synthesis and Apparent Bandgap of Nanophase Zirconia, *J Mater Sci Lett* (2000) 931–933, <https://doi.org/10.1023/A:1006799701474>.
 - [56] S.C. Middleburgh, W.E. Lee, M.J.D. Rushton, Structure and properties of amorphous uranium dioxide, *Acta Mater* 202 (2021) 366–375, <https://doi.org/10.1016/j.actamat.2020.10.069>.
 - [57] A. Garner, C. Gillen, G. Stephens, P. Styman, S. Armson, J. Robinson, J. Liu, A. Carruthers, F. Pickering, S. Sherry, C. Chan, M. Fenwick, H. Hulme, S. Ortnor, C. Riley, C. Grovenor, P. Frankel, S.C. Middleburgh, A. Cole-Baker, Mechanistically Understanding the Role of Lithium in Accelerated Corrosion of Zirconium Alloys Using Advanced Characterisation and Atomistic Simulation, *Press*, 2022.
 - [58] S.C. Middleburgh, S. Dumbill, A. Qaisar, I. Vatter, M. Owen, S. Valley, D. Goddard, D. Eaves, M. Puide, M. Limbäck, W.E. Lee, Enrichment of Chromium at Grain Boundaries in Chromia Doped UO₂, *Journal of Nuclear Materials* 575 (2023), 154250, <https://doi.org/10.1016/j.jnucmat.2023.154250>.
 - [59] P.V. Nerikar, K. Rudman, T.G. Desai, D. Byler, C. Unal, K.J. McClellan, S. R. Phillpot, S.B. Sinnott, P. Peralta, B.P. Uberuaga, C.R. Stanek, Grain Boundaries in Uranium Dioxide: Scanning Electron Microscopy Experiments and Atomistic

- Simulations, Journal of the American Ceramic Society. 94 (2011) 1893–1900, <https://doi.org/10.1111/j.1551-2916.2010.04295.x>.
- [60] J. Cízek, O. Melikhova, I. Procházka, J. Kuriplach, R. Kužel, G. Brauer, W. Anwand, T.E. Konstantinova, I.A. Danilenko, Defect studies of nanocrystalline zirconia powders and sintered ceramics, Phys Rev B 81 (2010), 024116, <https://doi.org/10.1103/PhysRevB.81.024116>.
- [61] S. Zhao, J. Xue, Y. Wang, S. Yan, Study on the effect of pressure on the properties of intrinsic point defects in monoclinic zirconia: *Ab initio* calculations, J Appl Phys 111 (2012), <https://doi.org/10.1063/1.3682766>.